Microsc. Microanal. 21, 190–203, 2015
doi:10.1017/S1431927614014615

Microscopy AND Microanalysis

Micro-Topography and Reactivity of Implant Surfaces: An *In Vitro* Study in Simulated Body Fluid (SBF)

M.G. Gandolfi,[1,*] P. Taddei,[1] F. Siboni,[1] V. Perrotti,[2] G. Iezzi,[2] A. Piattelli,[2] and C. Prati[1]

[1]*Department of Biomedical and NeuroMotor Sciences, University of Bologna - Via San Vitale 59 - 40126, Bologna, Italy*
[2]*Department of Medical, Oral and Biotechnological Sciences, University of Chieti-Pescara - Via dei Vestini 1 - 66100, Chieti, Italy*

Abstract: The creation of micro-textured dental implant surfaces possessing a stimulating activity represents a challenge in implant dentistry; particularly, the formation of a thin, biologically active, calcium-phosphate layer on their surface could help to strengthen the bond to the surrounding bone. The aim of the present study was to characterize in terms of macrostructure, micro-topography and reactivity in simulated body fluid (SBF), the surface of titanium (Ti) implants blasted with TiO_2 particles, acid etched with hydrofluoric acid, and activated with Ca and Mg-containing nanoparticles. Sandblasted and acid-etched implants were analyzed by ESEM-EDX (environmental scanning electron microscope with energy dispersive X-ray system) to study the micromorphology of the surface and to perform elemental X-ray microanalysis (microchemical analyses) and element mapping. ESEM-EDX analyses were performed at time 0 and after a 28-day soaking period in SBF Hank's balanced salt solution (HBSS) following ISO 23317 (implants for surgery—*in vitro* evaluation for apatite-forming ability of implant materials). Microchemical analyses (weight % and atomic %) and element mapping were carried out to evaluate the relative element content, element distribution, and calcium/phosphorus (Ca/P) atomic ratio. Raman spectroscopy was used to assess the possible presence of impurities due to manufacturing and to investigate the phases formed upon HBSS soaking. Micro-morphological analyses showed a micro-textured, highly rough surface with microgrooves. Microchemical analyses showed compositional differences among the apical, middle, and distal thirds. The micro-Raman analyses of the as-received implant showed the presence of amorphous Ti oxide and traces of anatase, calcite, and a carbonaceous material derived from the decomposition of an organic component of lipidic nature (presumably used as lubricant). A uniform layer of Ca-poor calcium phosphates (CaPs) (Ca/P ratio <1.47) was observed after soaking in HBSS; the detection of the 961 cm^{-1} Raman band confirms this finding. These implants showed a micro-textured surface supporting the formation of CaPs when immersed in SBF. These properties may likely favor bone anchorage and healing by stimulation of mineralizing cells.

Key words: apatite formation, element mapping, sand-blasted acid-etched surface, surface microanalysis, titanium endosseous dental implants

INTRODUCTION

Successful implantation of titanium (Ti) implants is strongly affected by biological events occurring at the bone-implant interface. In order to improve osseointegration and to accelerate the initial healing processes, a challenge is to achieve the formation of new bone in direct contact with the implant surface at early post-implantation periods. Many investigations have demonstrated that the presence of calcium phosphate (CaP) covering the surface of Ti implants improved and accelerated their integration with bone tissue (Cao & Hench, 1996; Narayanan et al., 2008; Aniket et al., 2012; Alghamdi et al., 2013; Gil et al., 2014).

Several physical and chemical methods have been used to put hydroxyapatite or CaPs onto metal surfaces, leading to bioactive fixation of the implant. Typically, physical techniques include plasma spraying deposition, physical vapor deposition, magnetron sputtering deposition, ion beam assisted deposition, pulsed laser deposition, and hot isostatic pressing. Chemical techniques include the sol-gel method, biomimetic processes, electrochemical deposition, micro-arc oxidation, and electrophoretic deposition (Aparicio et al., 2007; Ballo et al., 2011).

The biomimetic process is a physicochemical method in which a biologically active CaP covering is formed on a substrate after soaking in an acellular protein-free supersaturated calcium and phosphate simulated body fluid (SBF) with ion concentrations nearly equal to those of the inorganic part of human blood plasma (Wen et al., 1997; Bigi et al., 2005; Lu & Leng, 2005; BS ISO 23317, 2007). The deposition of apatite on Ti and Ti alloys depends on several factors such as composition of the Ti oxide layer, the presence of acidic or basic Ti-OH groups, and surface charge topography.

Technological research on endosseous Ti implants has been focused on the production of modified reactive surfaces able to rapidly nucleate biologically active CaP covering through treatments acting on the native oxide layer. Thermal treatment (heating) and/or exposure to alkaline or acidic solutions, such as sodium hydroxide (NaOH), hydrofluoric acid (HF), or other acids, can be used to transform the

Received June 27, 2014; accepted December 9, 2014

*Corresponding author. mgiovanna.gandolfi@unibo.it

different Ti oxide phases (amorphous oxides, Ti oxide, Ti dioxide polymorphs, i.e. rutile, anatase and brookite, non-stoichiometric oxides) and/or to corrode the Ti surface by dissolution of the oxide layer. Ti surfaces with different reactivity and topography can be obtained.

The aim of the present investigation was macroscopic and microscopic characterization of the surface of Ti implants blasted with TiO_2 particles, acid-etched with HF, and activated with Ca and Mg-containing nanoparticles. Specifically, screw design and pitch, thread shape, morphological and compositional characteristics, and the surface reactivity, i.e. nucleation of CaP when immersed in SBF, were assessed.

MATERIALS AND METHODS

Implants

Sandblasted and acid-etched endosseous dental implants 5.5 × 11 mm (Universal II Cone Morse, Implacil De Bortoli, Sao Paulo, Brazil) were studied.

Environmental Scanning Electron Microscope with Energy Dispersive X-ray System (ESEM-EDX) Microanalyses

Surface microanalyses were performed using an ESEM (Zeiss EVO 50; Carl Zeiss, Oberkochen, Germany) connected to a secondary electron detector for energy dispersive X-ray spectroscopy (EDS; Oxford INCA 350 EDS, Abingdon, UK) using computer-controlled software (Inca Energy Version 18, Abingdon, UK; Gandolfi et al., 2011*a*, 2013). The samples were examined uncoated at low vacuum (100 Pascal), accelerating voltage of 20 kV, working distance 8.5 mm, 0.5 wt% detection level, 133 eV resolution, amplification time 100 μs, measuring time: 600 s for element mapping and 60 s for spectra.

EDX microchemical analysis (elemental X-ray microanalysis) was carried out at random in areas of ~50 × 50 μm to evaluate the relative element content. The elemental microanalysis (weight % and atomic %) with ZAF correction method—a procedure in which corrections for atomic number effect (Z), absorption (A), and fluorescence (F) are calculated separately—was performed in full frame and spot mode to analyze entire areas or specific points, respectively. EDX element mapping was performed on the surface to detect the element distribution using a 512 × 384 pixel matrix, 30–40 frames, 100 μs dwelling time, and 600–700 μs total reading time.

EDX provides qualitative and semi-quantitative analysis of the elements.

Test in SBF

The International Standard ISO 23317 method (BS ISO 23317, 2007) was used to evaluate the formation of a layer rich in Ca and P (CaP covering) on the surface of the implants soaked in Hank's balanced salt solution (HBSS), which was used as SBF (Gandolfi et al., 2010, 2011*a*, 2013). The HBSS (Cambrex Bio Science Verviers, Belgium, cat. n.10–527) composition was: Ca^{2+} 1.27 mM, Cl^- 144.7 mM, K^+ 5.8 mM, Na^+ 141.6 mM, Mg^{2+} 0.81 mM, HCO_3^- 4.17 mM, SO_4^{2-} 0.81 mM, $H_2PO_4^-$ 0.44 mM and HPO_4^{2-} 0.336 mM). Each sample was placed vertically (BS ISO 23317, 2007) in 20 mL of HBSS at 37°C and uncoated surfaces were examined; surface microanalyses were performed by ESEM-EDX after a 28-day soaking period to assess the formation of CaPs. ESEM allowed visualization of the changes to the surface micro- and nano-morphology, and EDX measurements of atomic calcium and phosphorus percentages were used to calculate calcium/phosphorus atomic ratios. The Ca/P atomic ratio obtained from the outer surface of the samples was calculated and compared with the Ca/P ratio of apatitic and non-apatitic CaPs, namely Ca-poor apatite (Ca/P 1.5–1.67), Ca-poor non-apatitic CaPs (Ca/P ratio <1.47), Ca-rich (carbonated) apatite (Ca/P ratio 1.6–2.0) and Ca-rich non-apatitic CaPs (Ca/P 1.83) (Raynaud et al., 2002; Wang & Nanchollas, 2008). The formation of calcium carbonate ($CaCO_3$) polymorphs (calcite and aragonite) was taken into account in the presence of very high Ca/P ratios (Gandolfi et al., 2011*b*).

Raman Spectroscopy

Raman spectroscopy was used to assess the possible presence of impurities due to manufacturing and to investigate the phases formed upon HBSS soaking. To improve the detection of these components, a micro-Raman spectrometer was utilized.

Micro-Raman spectra were obtained using a Jasco NRS-2000C instrument (Jasco Inc., Easton, MD, USA) connected to a microscope with 100× magnification and a 160 K frozen CCD detector (Spec-10: 100B, Roper Scientific Inc., Trenton, NJ, USA). The spectra were recorded in backscattering conditions with 1 cm^{-1} spectral resolution using an objective lens of 100× magnification and a 532 nm Green Diode Pumped Solid State (DPSS) Laser Driver (RgBLase LLC, Fremont, CA, USA) with a power of about 5 mW. This instrument setup allowed a circular sampling area with a 1 μm diameter.

The chosen conditions prevented any sample transformation. Actually, when using a 100× magnification and laser power values higher than 5 mW the formation of Ti oxide as rutile polymorphic form was detected.

To obtain a good representation of the analyzed implants, at least 30 micro-Raman spectra were collected in different points of each sample.

The micro-Raman analysis was completed with FT-Raman characterization, which allowed the investigation of wider sample areas (the focused laser beam diameter was about 100 μm). FT-Raman spectra were recorded on a Bruker MultiRam FT-Raman spectrometer equipped with a cooled Ge-diode detector. The excitation source was a Nd^{3+}-YAG laser (1,064 nm) in the backscattering (180°) configuration, and spectral resolution of 4 cm^{-1}. The reported spectra were recorded with a laser power at the sample of about 60 mW. No sample degradation upon laser irradiation under these conditions was observed.

RESULTS

As-Received Implants (Time 0)

ESEM-EDX Microanalyses

Collar : ESEM-SE macromorphology of the upper portion of the prosthetic screw shows a four-sided polygonal profile with a microrough surface (Fig. 1a). The spires appeared differentiated in thickness but not in depth, with increasing thickness from ~20 to 200 μm going from the apical to the distal/neck portion. The entire body of the prosthetic screw and the surfaces of the spires showed a rough surface. At higher magnification, the surface of the neck/collar appeared machined and entirely streaked by parallel grooves and prominences having a peak-to-peak distance of about 10 μm (Figs. 1b, 1c). The microstructure of the surface in the collar region was well evident at high resolution (Fig. 1d). Flakes/scales with sharp edges could be noticed. EDX microanalysis revealed carbon (C), oxygen (O), aluminum (Al), Ti (Ti), vanadium (V) and iron (Fe) (Fig. 1e) and their weight and atomic percent (Table 1a), and EDX elemental mapping showed their distribution on the implant surface (Fig. 1f). ESEM-BSE pictures showed the topography and 3D morphology of the pits/porosities and coarseness/protrusions (Figs. 2a–2d).

Body: In the middle portion of the implant body, reduction of the thread thickness from about 200 to 100 μm, going towards the apex, was evident (Fig. 3a). At high magnification, the micro and nano-irregularities of the surface were visible. The topography showed rounded peaks/irregularities (Figs. 3b, 3c). At even higher magnification, the details of the rough surface morphology could be distinguished and roughened coarseness (pits and flakes) spaced out with porosities and depressions were present (Fig. 3d). Micropits on the Ti surface had sizes ranging from 0.5 to 2 μm in diameter. Nanoscale topographical changes of

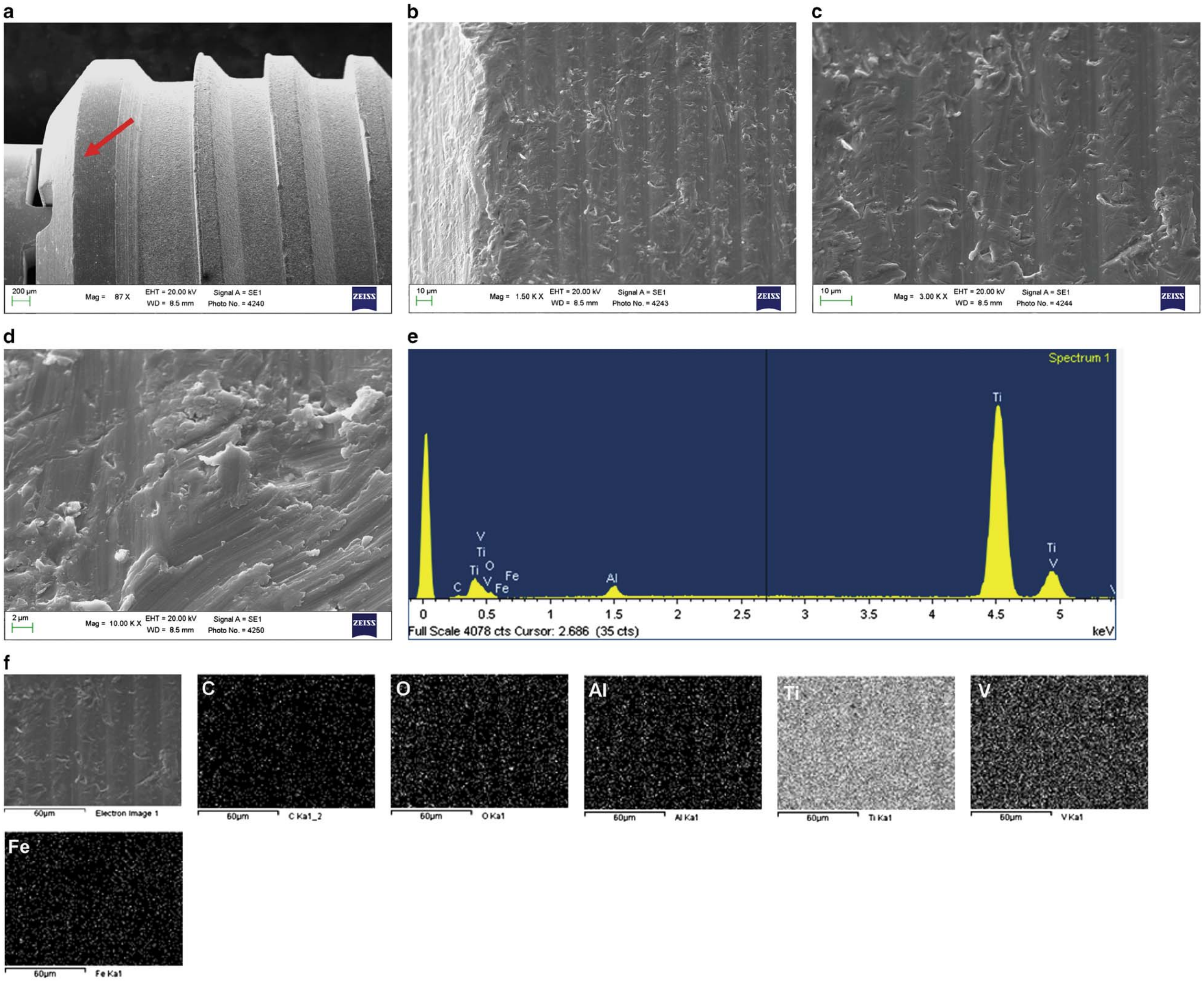

Figure 1. ESEM-SE and EDX analyses of the collar portion at Time 0 (as-received). C, O, Al, Ti, V and Fe are displayed in EDX elemental maps (f).

Table 1. Microanalysis (weight % and atomic %) of the collar (a, d), body (b, e) and apex (c, f) of the as-received implant surface (a-c) and after 28-day soaking in HBSS (d–f).

Element	Weight %	Atomic %
(*a*)		
C K	2.25	6.42
O K	15.68	33.64
Al K	2.16	2.74
Ti K	78.78	56.45
V K	0.71	0.48
Fe K	0.43	0.26
Total	100.00	
(*b*)		
C K	1.25	4.81
Ti K	98.75	95.19
Total	100.00	
(*c*)		
C K	1.92	5.56
O K	15.13	32.89
Al K	2.37	3.05
Ti K	80.28	58.30
Fe K	0.31	0.19
Total	100.00	
(*d*)		
C K	1.69	3.80
O K	34.63	58.44
Na K	1.75	2.06
Mg K	0.26	0.29
P K	1.20	1.04
Cl K	0.68	0.52
Ca K	1.36	0.92
Ti K	58.43	32.93
Total	100.00	
(*e*)		
C K	3.40	7.37
O K	35.19	57.18
Na K	1.27	1.44
Mg K	0.33	0.35
Al K	1.13	1.09
P K	1.43	1.20
Cl K	0.61	0.45
Ca K	1.81	1.18
Ti K	54.82	29.75
Total	100.00	
(*f*)		
C K	2.05	4.57
O K	32.88	55.02
Na K	4.01	4.67
Mg K	0.25	0.27
Al K	1.02	1.01
P K	1.35	1.17
Cl K	2.29	1.73
Ca K	1.57	1.05
Ti K	54.57	30.50
Total	100.00	

this surface compared with that of the collar region were evident. X-ray microprobe analysis revealed the presence of Ti (95.19 atomic %) and C (4.81 atomic %) (Fig. 3e, Table 1b). EDX elemental mapping showed the homogeneous distribution of the constitutive elements (Fig. 3f). ESEM-BSE images displayed the surface roughness (Figs. 2e–2h).

Apex (screw tip): Macrolevel analyses showed a hemispheric apex with thin lamellae spaced at $\sim$400 μm (Fig. 4a). The surface was visibly coarse with rounded protruding irregularities; its structure at the nanolevel showed rounded pits and flakes (Figs. 4b–4d). Nanomorphology of the apex and body portions was the same, while differences were observed in surface chemistry. EDX detected Ti (58.30 atomic %) and C (5.56 atomic %) but also O (15.13 atomic %), Al (3.05 atomic %), and traces of Fe (0.19 atomic %) (Fig. 4e, Table 1c). Elemental mapping showed the distribution of the constituents (Fig. 4f). ESEM-BSE pictures showed the surface coarseness and hollows (Figs. 2i–2n).

Raman analyses

Figure 5a (top) shows some representative micro-Raman spectra recorded on the as-received implant.

Pure metals do not have any Raman spectra; therefore, this technique was used to assess the possible presence of impurities other than pure metals, due to manufacturing. To improve the detection of such granules, the highest magnification available was used (i.e., 100×, which corresponds to a circular sampling area with a 1 μm diameter).

Most of the obtained spectra were similar to that reported in Figure 5a, trace a; this spectrum appeared dominated by the bands of the laser, although two broad bands at about 1,590 and 1,350 cm^{-1}, assignable to the stretching vibrational modes of C-C bonds of inorganic nature (Tuinstra & Koenig, 1970) were detected. In some spectra, these C-C bands were superimposed to those at about 1,740 and 1,445 and 1,300 cm^{-1}, ascribable to an organic component (Fig. 5a, trace 1d).

Some spectra appeared more similar to that reported in Figure 5a, trace b; this spectrum showed an ascending baseline in the wavenumber region between 800 and 400 cm^{-1}. This spectral feature would suggest the presence of amorphous Ti oxide (Aggour et al., 2005). This hypothesis is confirmed by the spectrum recorded at a laser power of 10 mW (Fig. 5a, trace c): the bands of rutile at 608 and 409 cm^{-1} appeared, suggesting that amorphous Ti oxide transforms into a crystalline phase, in agreement with other authors (Kilpadi et al., 1998).

Besides the broadening due to amorphous Ti oxide, some spectra (Fig. 5a, trace 1e) also showed a weak band at 138 cm^{-1}, which could be ascribed to anatase (Ohsaka et al., 1978). The weakness of this band suggests that traces of this phase should be present (or, in other words, its thickness is not enough to be detected by Raman spectroscopy).

Other spectra (Fig. 5a, trace f) showed the presence of calcium carbonate, mainly as calcite, as revealed by the bands at 1,088 and 713 cm^{-1} (Martinez-Ramirez et al., 2003).

Implants Soaked in HBSS (Time 28 days)

ESEM-EDX Microanalyses

Collar: After 28 days in HBSS, the surface observed by ESEM in wet conditions appeared fairly different from that at $t = 0$

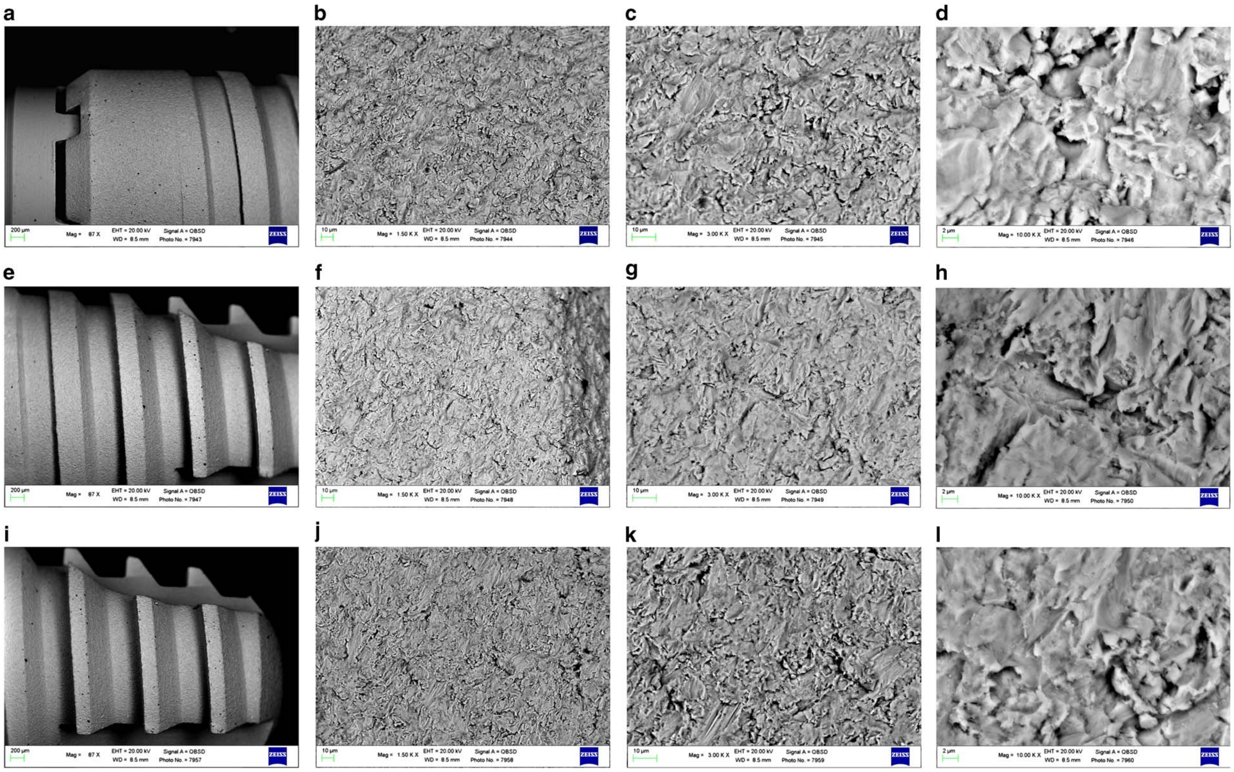

Figure 2. ESEM-BSE analyses of the different implant portions - collar (a–d), body (e–h) and apex (i–n) - at Time 0 (as-received).

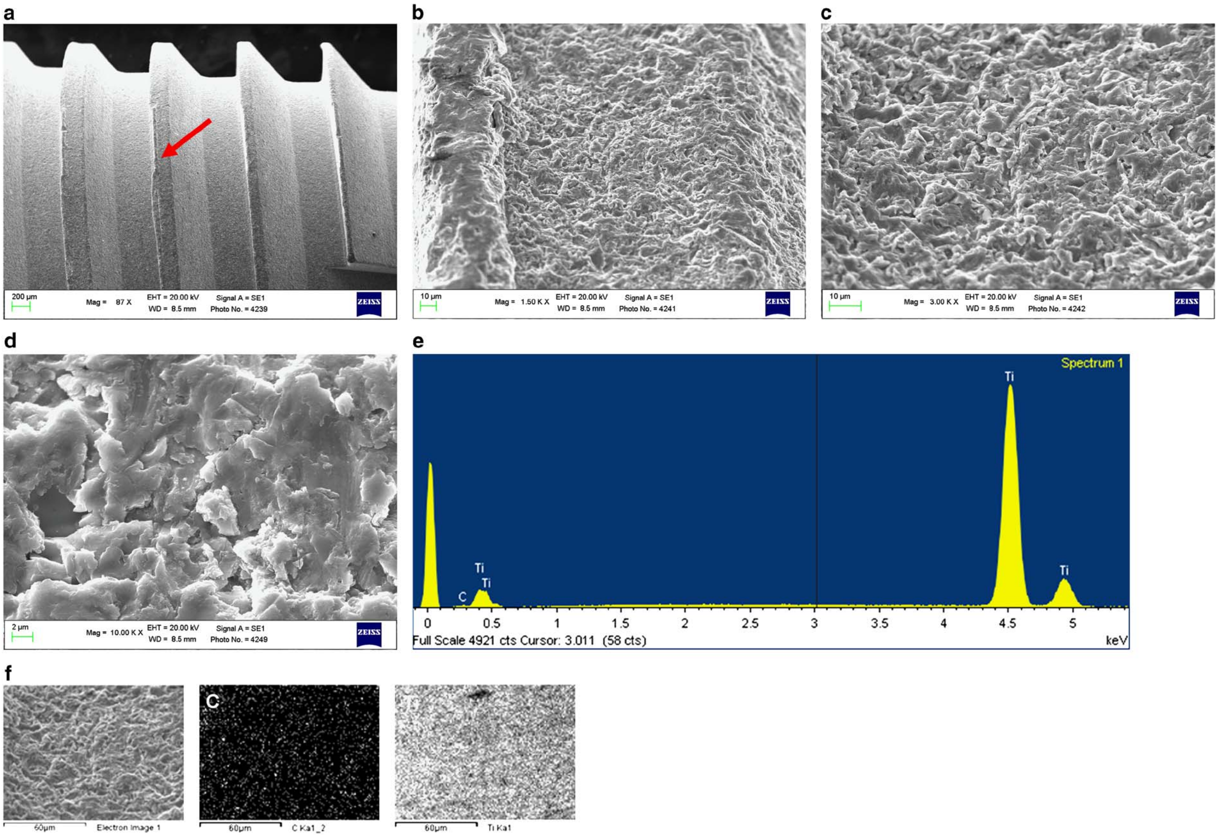

Figure 3. ESEM-SE and EDX analyses of the body portion at Time 0 (as-received). EDX element mapping of C and Ti are reported (f).

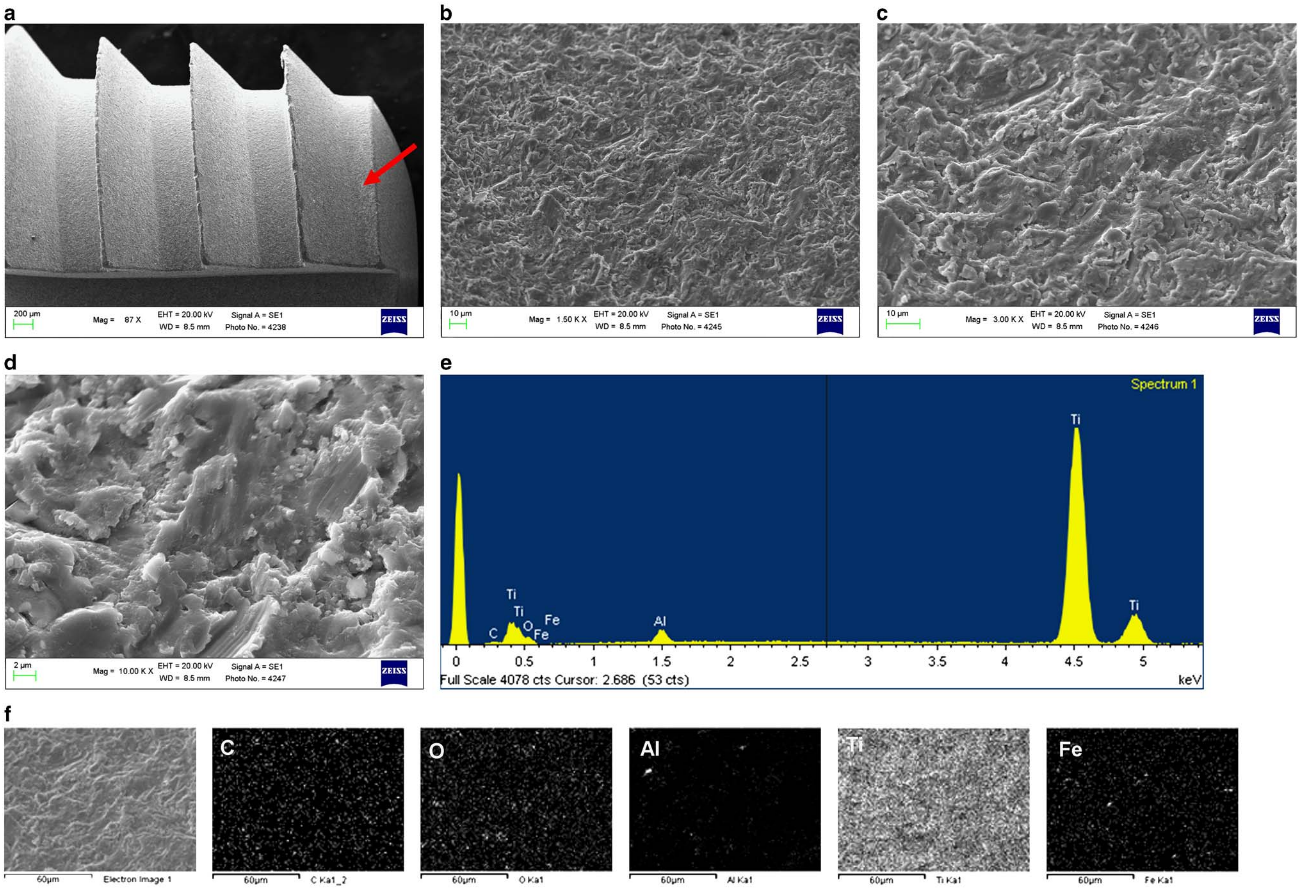

Figure 4. ESEM-SE and EDX analyses of the apical portion at Time 0 (as-received). EDX maps of C, O, Al, Ti and Fe are shown (f).

and the soaking in HBSS appeared to smooth out/level and soften the topography at a micrometer scale roughness. The parallel grooves were still visible, but the pits and flakes appeared smooth and less prominent (Figs. 6a–6c). Scattered white deposits were found on the surface; at high resolution they appeared globular or composed by the aggregation of smaller spherulitic deposits (Fig. 6d). EDX detected C, O, and Ti together with new elements as Na, Mg, P, Cl, and Ca (Fig. 6e, Table. 1d). No traces of V nor Fe were detected. The Ca/P atomic ratio calculated on the entire area was about 1.13. Element mapping showed the homogeneous distribution of the deposits, in particular the uniform coating of Ca and P (Fig. 6f). ESEM-BSE analyses of the topography and 3D morphology showed the reduction and/or disappearance of pits and porosities and surface smoothening (Figs. 7a–7d).

Body: After soaking in HBSS the surface of the body also appeared less rough (Figs. 8a–8d). The surface showed a mild/gentle roughness; peaks and irregularities seemed to be smoothed and softened. EDX revealed C, O, and Ti but also Al, Na, Mg, P, Cl, and Ca that were absent in fresh samples (Fig. 8e, Table 1e). The Ca/P atomic ratio calculated on the entire area was about 1.27. Element mapping displayed the uniform presence of deposited Ca and P. No traces of V nor Fe were detected (Fig. 8f). ESEM-BSE analyses showed smoothening of the surface with reduction of the micro- and nano-roughness through the over deposition of material (Figs. 7e–7h).

Apex (tip): For the apical region (Fig. 9a), soaking in HBSS changed the surface feature in terms of lesser roughness (Figs. 9b, 9c), presence of deposits (Fig. 9d), and surface chemistry (Figs. 9e–9f, Table 1f). EDX showed C, O, Al, and Ti and also Na, Mg, P, Cl, and Ca that were absent in fresh samples (Fig. 9e, Table 1f). No traces of Fe were detected. The Ca/P atomic ratio calculated for the entire area was ~1.16. Element mapping displayed the distribution of the elements, in particular the homogeneous deposition of Ca and P (Fig. 9f). ESEM-BSE analyses showed softening of the surface coarseness and reduction of the porosities, as in the body region (Figs. 7i–7n).

Raman analyses

Figure 5b (bottom) shows some representative spectra recorded on the implant soaked in HBSS. As observed for the as-received sample, most spectra revealed the presence of C-C bonds of inorganic nature and were similar to that reported in Figure 5a, trace a.

The spectrum reported in Figure 5b, trace a showed the bands of a long-range well ordered calcite phase, as revealed by the presence of the lattice band at 275 cm^{-1}, besides those mentioned above at 1,092 and 713 cm^{-1} (Martinez-Ramirez

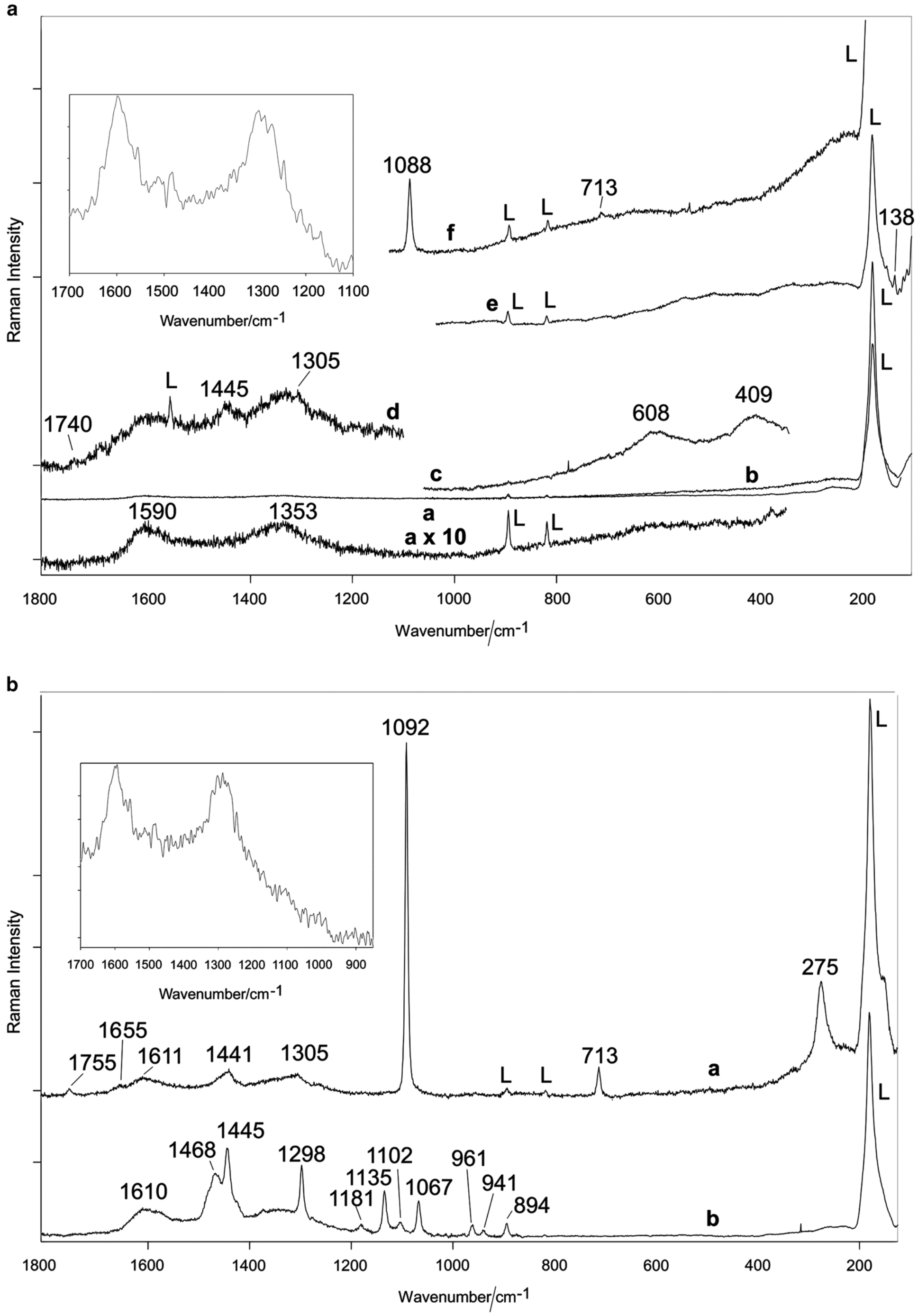

Figure 5. (a, top) Representative micro-Raman and FT-Raman (inset) spectra recorded on the surface of the as-received implant: (a), (b), (d), (e) and (f): recorded at a laser power of 5 mW; (c) recorded at a laser power of 10 mW. (b, bottom) Representative micro-Raman and FT-Raman (inset) spectra recorded on the surface of the implant soaked in HBSS (laser power 5 mW).

et al., 2003). The bands of calcite were superimposed to those at 1,755, 1,655, 1,611, 1,441, and 1,305 cm^{-1}, assignable to an organic component, probably of lipidic (fat) nature (Vandenabeele et al., 2000; Baranska et al., 2011).

The bands observed in Figure 5b, trace b at 1,610, 1,468–1,445, 1,258, 1,181, 1,135, 1,102, 1,067, 941, and 894 cm^{-1} are observable at similar wavenumber values in stearate salts (De Veij et al., 2009); the band at 961 cm^{-1}, observed only in the reported spectrum, is compatible with the presence of a CaP phase (Nelson et al., 1982; Taddei et al., 2000).

DISCUSSION

Implants investigated in the present study showed a sand-blasted surface, etched with HF and activated with Ca and

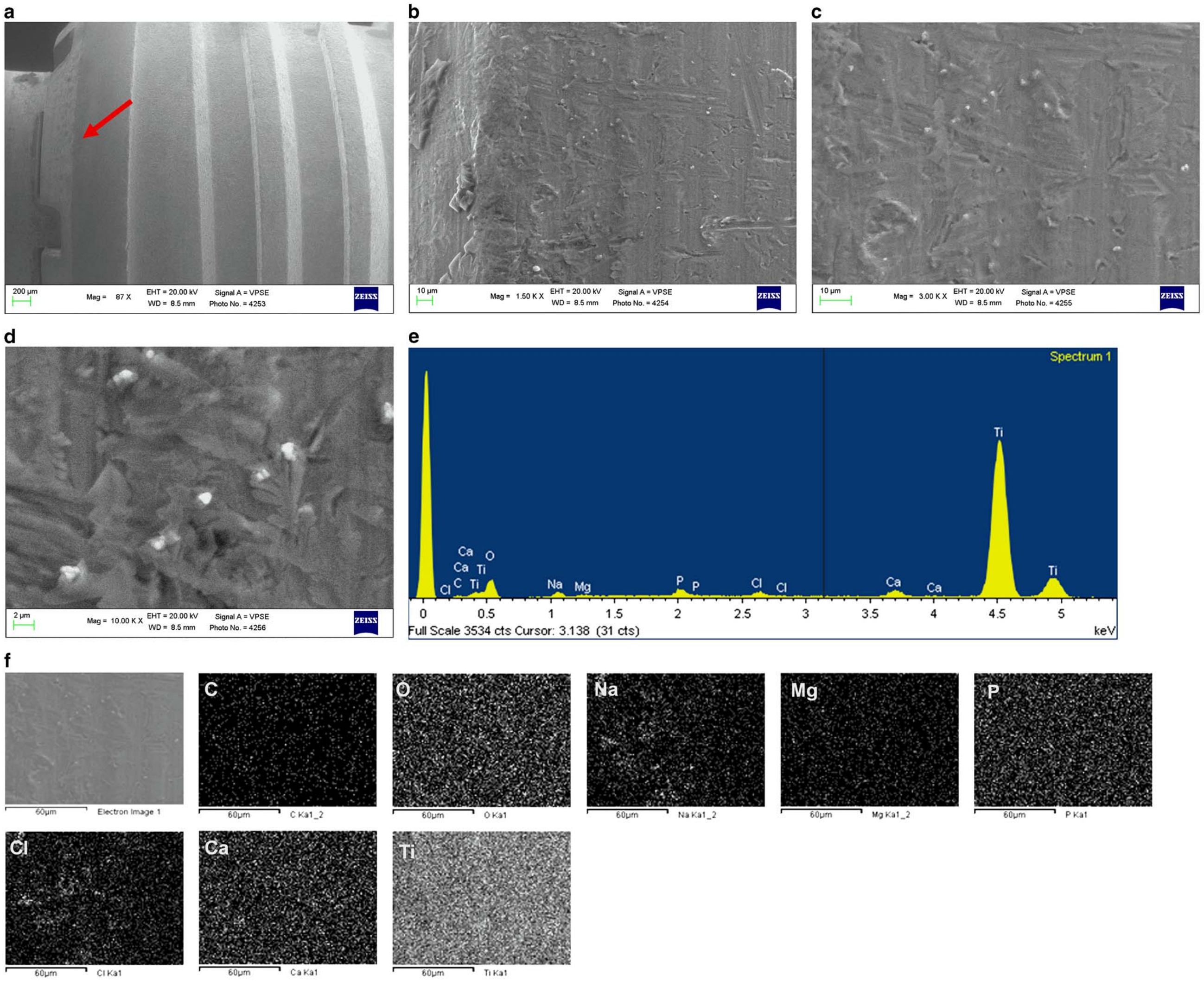

Figure 6. ESEM-SE (a-d) and EDX (e) analyses of the collar portion after 28-day soaking in HBSS. C, O, Na, Mg, P, Cl, Ca and Ti are displayed in EDX maps (f).

Mg nanoparticles (Iezzi et al., 2012; Gehrke et al., 2013; Piattelli et al., 2014). Both blasting and acidic treatments were likely performed to modify the surface and obtain a tailored micro-/nano-scale roughness to improve osteoblastic behavior and osseointegration (Guo et al., 2007; Khang et al., 2008; Kubo et al., 2009; Tsukimura et al., 2011).

Blasting is a technique that leads to the creation of a porous layer on the implant surface achieved through collision with microscopic blasting particles, such as Ca, Fe, Mg, P, quartz (Si), V, and others (Hubbs et al., 2001), shot at the surface. Debris and blasting residuals of the collided particles are often found on the blasted surfaces in SEM observations (Massaro et al., 2002; Kang et al., 2009) and in surface chemistry analysis (Massaro et al., 2002). In the present study, potential blasting residuals were found in the collar and apex regions, but not in the body of the implant of the fresh surfaces.

Etching treatments with HF-containing solutions (HF) were used as roughening procedures to form a porous layer on the surface. When Ti was exposed to HF solutions, fluoride (F –) from the dissociated HF reacted with the oxide of the TiO_2 layer that rapidly dissolved and then penetrated through the Ti lattice defects. Therefore, in the TiO_2–HF–H_2O system, Ti was rapidly attacked and underwent corrosion and erosion. Ti fluorides such as soluble Ti trifluoride (TiF_3), Ti tetrafluoride (TiF_4) (Straumanis & Chen, 1951), and Ti oxyfluoride ($TiOF_2$) (Busalev et al., 1962) were formed. In the present study, high-resolution ESEM observations in both the body and apex regions showed a nanolevel surface topography with micro- and nano-rounded coarseness (flakes and micropits) spaced out with porosities and depressions consistent with the acid treatment. Differently, the neck/collar appeared machined and entirely streaked by parallel grooves and prominences, with flakes/scales with sharp edges indicating a lack of the corrosive acidic treatment in that area. No traces of F were detected by microanalysis on the implant surface, likely due to short HF treatment and/or low concentrations of solutions, in agreement with a previous study (Lamolle et al., 2009*a*, 2009*b*). No Ti fluorides were detected by Raman spectroscopy.

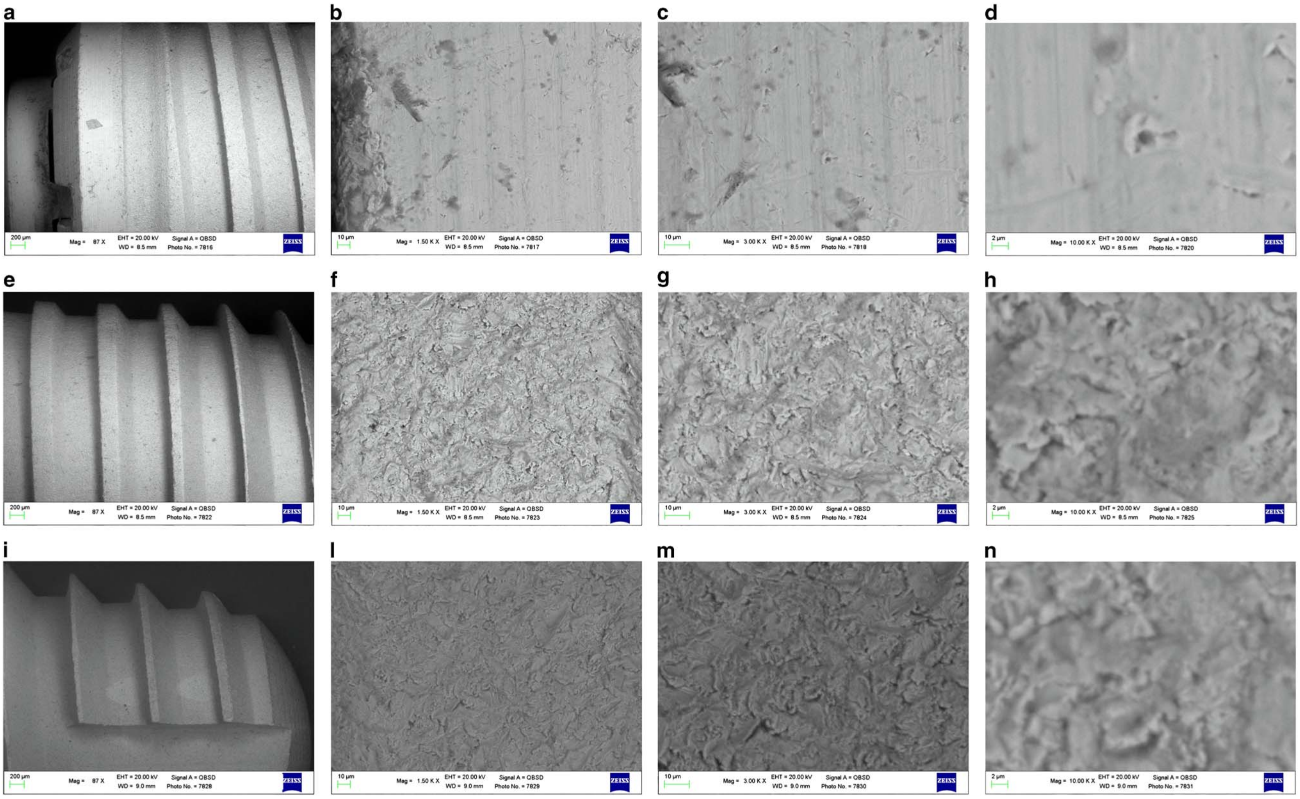

Figure 7. ESEM-BSE analyses of the different implant portions - collar (a–d), body (e–h) and apex (i–n) - at Time 28d in HBSS.

The surface nano-featuring of endosseous Ti implants is clinically relevant. Studies revealed the potential of nano-featured Ti surfaces in inducing cell-specific affinity, e.g. selective attractiveness for osteogenic cells, but not fibroblasts (Masaki et al., 2005; Variola et al., 2008; Biggs et al., 2009, 2010; Kubo et al., 2009; Hori et al., 2010) and that the increased surface topography of Ti implants improved the bone-to-implant contact and mechanical properties of the enhanced interface (Cooper, 2000) and the osseointegration of the implant (Le Guèhennec et al., 2007). Interestingly, in the present investigation, notable differences among the collar–body–apex of the fresh implant were found in both the micromorphological ESEM results and in the microchemical EDX data. In addition to Ti, microanalysis revealed amounts of C, O, Al, and traces of V and Fe in the collar of fresh Ti implants while only C was noticed in the body and C, O, Al, and traces of Fe in the apex.

Ti alloys are preferred to pure Ti due to their better mechanical properties and corrosion resistance. Alloying elements are mainly alpha-stabilizers such as Al, O, N, C or beta-stabilizers such as Mo, V, Fe, Si, H (Liu et al., 2004). Carbon in Ti implants could also be a remnant or a surface contaminant from the manufacturing (i.e., from lubricants) or sterilization process (plastic packaging or supercritical carbon dioxide-based sterilization).

The detection of oxygen together with Al, V, and Fe in EDX analysis allowed speculation concerning the presence of oxides or hydroxides of these elements. Raman spectroscopy allowed exclusion of this possibility and suggested that Fe, Al, and V should be present as pure metal or alloying elements. On the other hand, the spectroscopy analysis showed the presence of amorphous Ti oxide/anatase phases, which account for the detection of oxygen in the EDX analysis.

Granules of calcite were detected by micro-Raman spectroscopy; the presence of this phase could be justified by considering that the particles used for sand blasting contained Ca (probably as calcium oxide which spontaneously reacts with carbon dioxide, producing calcium carbonate).

Most spectra recorded on the as-received implant showed the presence of bands at about 1,590 and 1,350 cm^{-1} assignable to the vibrational modes of C-C bonds of inorganic nature. These bands may be ascribed to C-C bonds present in the alloy (Racine et al., 2001), but it cannot be excluded that they are assignable to a charcoal component produced during manufacturing upon decomposition of the organic component of fat detected on the surface of the implant. Detection of the 1,590 and 1,350 cm^{-1} bands due to laser heating can be excluded since they were also observed at a laser power as low as 0.5 mW.

The latter interpretation was confirmed by the analysis of "control" Ti plates analyzed before the sand blasting treatment; no bands at 1,590 and 1,350 cm^{-1} were detected either in the FT-Raman or in the micro-Raman spectra. The latter revealed the presence of the same organic components detected in the micro-Raman spectra of the implants under study (spectra not shown). Actually, the micro-Raman

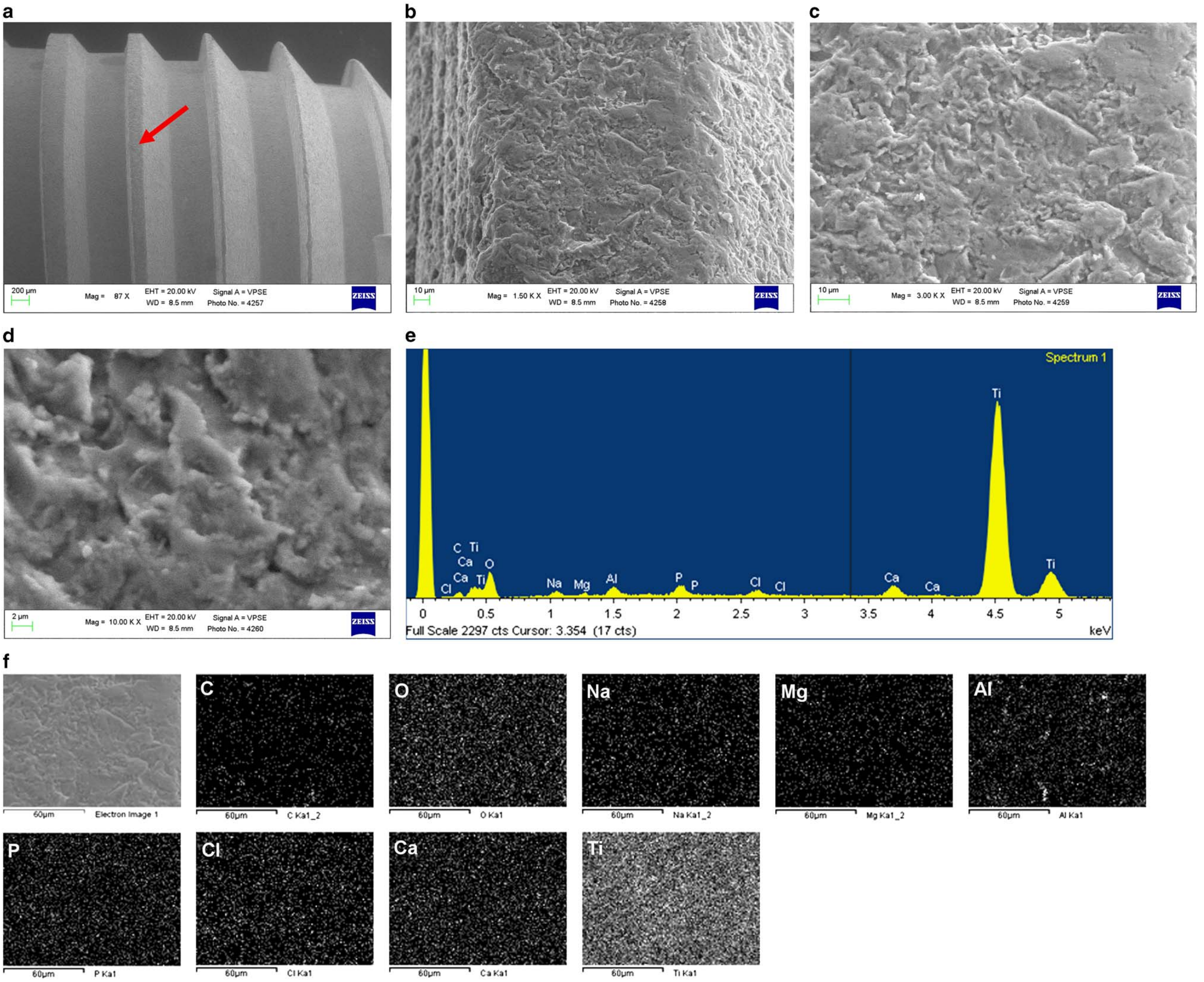

Figure 8. ESEM-SE (a–d) and EDX (e) analyses of the body portion after 28-day soaking in HBSS. EDX elemental mapping of C, O, Na, Mg, Al, P, Cl, Ca and Ti are represented (f).

spectra reported here showed that manufacturing appeared to decompose most of the organic component, although some residuals were detected. The conspicuous presence of C-C bonds of inorganic nature was confirmed by the detection of their marker bands, also by FT-Raman spectroscopy (Figs. 5a, 5b, insets).

After 28 days of soaking in HBSS, the surface morphology and the microcompositional data differed widely from that detected on the virgin surface. The HBSS was a saline water solution supersaturated towards apatite having a physiological-like pH (pH 7.4). The present study demonstrated the ability of the tested implants to nucleate CaPs on their surface. For reactions occurring at the Ti surface, it is well known that a passively protecting Ti oxide layer/coating forms on Ti and Ti-alloy surface when exposed to the air (atmospheric oxygen O_2) and water. This Ti oxide layer protects the metal against corrosion (Textor et al., 2011). In an aqueous electrolyte, such as body fluid or saliva, the TiO_2 molecule on the Ti surface becomes a dipole with positive Ti^+ and negative O^- sites. TiO_2 reacts with water and titanol groups (Ti-OH) form. Ti-OH groups exhibit/possess both acid and base or alkaline (amphoteric) properties depending on the pH of the surrounding solution: negative charges $[TiO]^-$ and positive charges $[TiOH_2]^+$ form in basic and acidic water solutions, respectively. In the present study, we speculate that when immersed in SBF, Ti oxide rapidly hydrates and Ti-OH groups form. As HBSS has a pH of 7.4, both acidic or basic Ti-OH groups (and therefore negatively and positively charged sites) coexist on the Ti surface. Hydroxyl groups exposed on the surface, although not revealed by Raman spectroscopy, probably due to the prevalently amorphous nature of Ti oxide, are responsible for the surface activity and are involved in nucleation of CaPs in serum-like environments. Therefore, each Ti site is able to immediately adsorb via electrostatic interaction both negatively charged phosphate ions ($H_2PO_4^-$ and HPO_4^{2-}) and positively charged calcium ions (Ca^{2+}, Na^+, Mg^{2+}) from the surrounding HBSS, and calcium titanate and Ti phosphate can form on the hydrated TiO_2 layer. It is

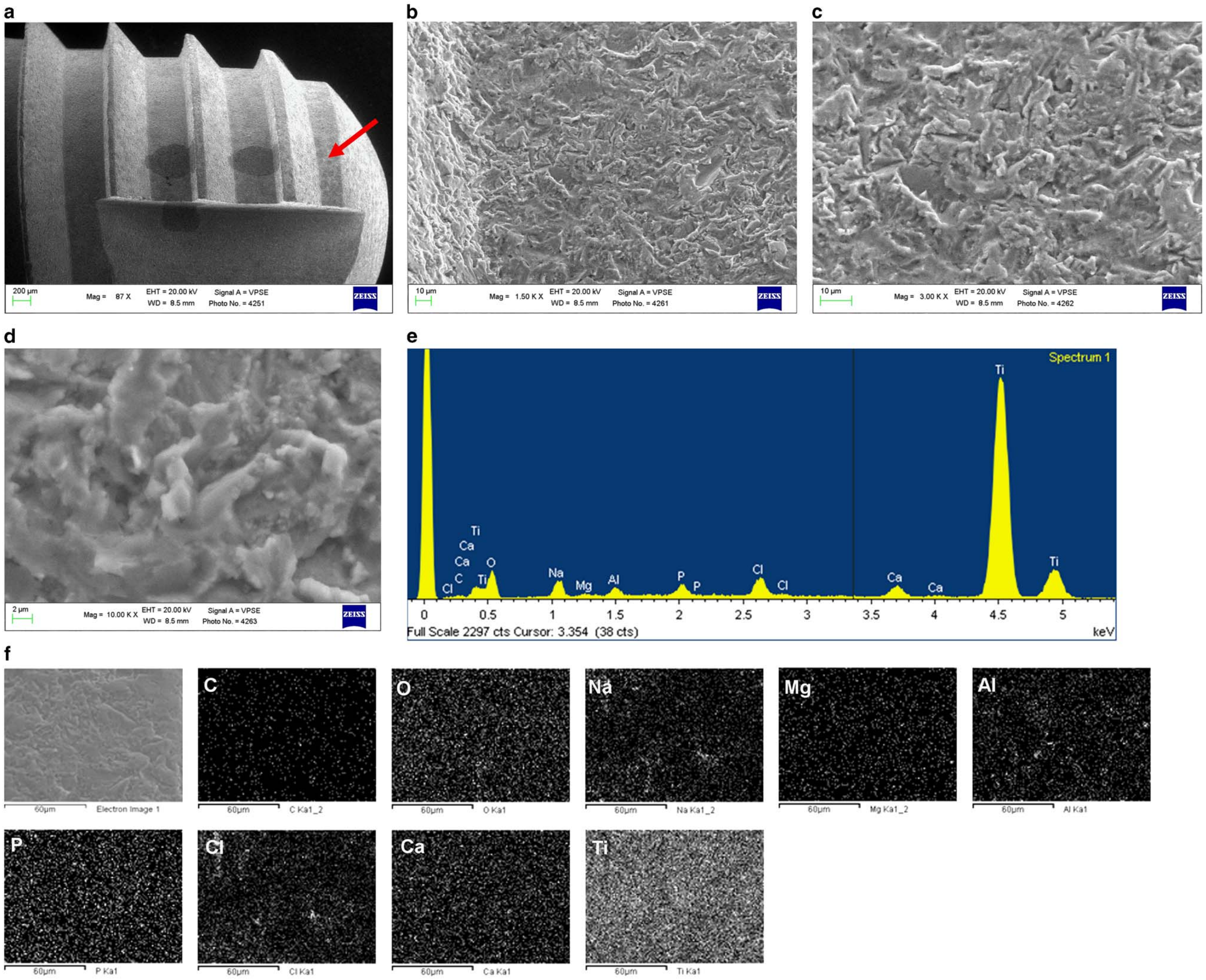

Figure 9. ESEM-SE (a–d) and EDX (e) analyses of the apical portion at Time 28d in HBSS. EDX map of C, O, Na, Mg, Al, P, Cl, Ca and Ti are shown (f).

possible to speculate that positive calcium and negative phosphate charges soon neutralize, consequently the CaP covering cannot grow into a thick layer in a short time. Actually, in the present study a thin film of CaPs uniformly covered the surface after 28 days in HBSS through the defined biomimetic coating process in SBF. Neither calcium titanate nor Ti phosphates were detected by Raman spectroscopy. The thinness of the CaP deposit was also demonstrated by this technique. In fact, only one micro-Raman spectrum recorded on the surface of the soaked implant showed the band at 961 cm^{-1}, due to the phosphate vibrational mode of CaP (Fig. 5b, trace b). Moreover, this band was not detected in the FT-Raman spectrum of the same sample (Fig. 5b, inset).

Our EDX data of the surface provided Ca/P ratios ranging from ~1.13 to 1.27, values consistent with the presence of amorphous CaPs (Ca/P 1.2–2.2), dicalcium phosphate (Ca/P ~ 1), tricalcium phosphate (Ca/P 1.33–1.5) and octacalcium phosphate (Ca/P 1.23). It is well known that the *in vitro* and *in vivo* precipitation of CaPs do not directly boost the growth of an apatite structure, but involves the initial formation of (amorphous) metastable CaPs that are precursors of apatite (Eanes et al., 1965; Takadama et al., 2001*a*, Wopenka & Pasteris, 2005), which gradually transform to bone-like apatite (Takadama et al., 2001*a*, 2001*b*; Gandolfi et al., 2011*b*).

The ability to nucleate CaP on Ti surfaces through the formation of titanol Ti-OH groups, has been demonstrated for Ti surfaces (Hanawa et al., 1997). Several studies demonstrated that Ca^{2+} is the first ion adsorbed by Ti surface when CaP forms (Tanahashi & Matsuda, 1997; Yang et al., 1999) and interestingly various Ti oxide phases with different types and density of hydroxyl groups showed different abilities in nucleating CaP deposition. As an example, anatase is speculated to have a higher ability to form apatite than rutile due to the higher acidity and the larger number of hydroxyl groups (Svetina et al., 2001).

It is clinically important to know whether a Ti surface of endosseous implants can be spontaneously coated by a film of CaPs through a biomimetic process when in contact with biofluids, owing to its intrinsic chemical–physical properties interlinked with its chemical composition and surface treatments. The rapid nucleation and layering of CaPs could be clinically responsible for improved bone formation and bone-implant integration. The adsorption of calcium and phosphate ions on the oxide layer creates nucleation sites for the formation and then growth of bone apatite-like crystals (carbonate hydroxyapatite) at the bone–implant interface. The bone apatite-like layer serves as a template for cell migration, differentiation, and bone growth at the implant–tissue interface, enhancing bone fixation and minimizing micromovements (Hench & Wilson, 1984). Thus, the oxide layer plays a key role in enhancing bioactivity and osseointegration of Ti or Ti-alloy implants.

In addition, the surface charge caused by TiO_2/H_2O reaction affects the adsorption of proteins and other charged macromolecules. Adsorbed proteins are essential for cell attachment to biomaterial surfaces (Degasne et al., 1999). Evaluation of the apatite-forming ability on implant materials in SBF is useful for preliminary evaluation of the biointeractivity (ability to exchange information with a biological system) and bioactivity (having an effect and cause a positive reaction in the host tissues), and to predict their *in vivo* bone-bonding ability (BS ISO 23317, 2007).

A bioactive surface stimulates cell attachment, differentiation and bone matrix synthesis (Muzzarelli et al., 1997) leading to an increased bone-implant contact in a shorter time, accelerating the process of bone implant contact formation, and providing the implant with increasing secondary stability at the earliest stages of healing.

It has been demonstrated that the addition of a hydroxyapatite coating to microroughened Ti accelerated and enhanced the level of bone-implant integration by increasing the osteoconductivity and inhibiting the soft tissue infiltration (Yamada et al., 2012).

Conclusion

In conclusion, the present micro-textured surface supported the formation of CaPs when immersed in SBF. These properties may likely favor bone anchorage and healing by biostimulation of mineralizing cells.

Acknowledgments

This study was supported by the institutional funds of Prof. Carlo Prati from RFO 2011 and 2012 and from the Master Program in Clinical Endodontics of the University of Bologna, Italy. The study was managed in the Laboratory of Biomaterials and Oral Pathology of the Dental School of the University of Bologna, Italy.

References

Aggour, M., Dittrich, T., Belaidi, A., Sieber, I. & Rappich, J. (2005). Anodic preparation of porous TiO_2 in fluoride solution. *Phys Stat Sol (c)* **2**, 3344–3348.

Alghamdi, H.S., Cuijpers, V.M., Wolke, J.G., van den beucken, J.J. & Jansen, J.A. (2013). Calcium-phosphate-coated oral implants promote osseointegration in osteoporosis. *J Dent Res* **92**, 982–988.

Aniket, Young, A., Marriott, I. & El-ghannam, A. (2012). Promotion of pro-osteogenic responses by a bioactive ceramic coating. *J Biomed Mater Res A* **100**, 3314–3325.

Aparicio, C., Manero, J.M., Conde, F., Pegueroles, M., Planell, J.A., Vallet-regí, M. & Gil, F.J. (2007). Acceleration of apatite nucleation on microrough bioactive Ti for bone-replacing implants. *J Biomed Mater Res A* **82**, 521–529.

Ballo, A.M., Omar, O., Xia, W. & Palmquist, A. (2011). Dental implant surfaces – physicochemical properties, biological performance, and trends, chapter 2. pp. 19–57 In *Implant Dentistry – A Rapid Evolving Practice*, Ilser T., ISBN 978-953-307-658-4, Tech publisher, Rijeka, Croatia. pp. 19–57.

Baranska, M., Schulz, H., Strehle, M. & Popp, J. (2011). Applications of vibrational spectroscopy to oilseeds analysis. In *Applications of Vibrational Spectroscopy in Food Science,* vol. 1, Li-Chan, E., Chalmers, J. & Griffiths, P. (Eds.), p. 414. John Wiley & Sons, Inc., Hoboken, NJ

Biggs, M.J., Richards, R.G. & Dalby, M.J. (2010). Nanotopographical modification: A regulator of cellular function through focal adhesions. *Nanomedicine* **6**, 619–633.

Biggs, M.J., Richards, R.G., Gadegaard, N., Mcmurray, R.J., Affrossman, S., Wilkinson, C.D., Oreffo, R.O. & Dalby, M.J. (2009). Interactions with nanoscale topography: Adhesion quantification and signal transduction in cells of osteogenic and multipotent lineage. *J Biomed Mater Res A* **91**, 195–208.

Bigi, A., Boanini, E., Bracci, B., Facchini, A., Segatti, S.P.F. & Sturba, L. (2005). Nanocrystalline hydroxyapatite coatings on Ti: A new fast biomimetic method. *Biomaterials* **26**, 4085–4089.

BS ISO 23317 (2012). Implants for surgery – In vitro evaluation for apatite-forming ability of implant materials. International Standard ISO/FDIS 23317:2012.

Busalev, Y.A., Bochkareva, V.A. & Nikolaev, N.S. (1962). The reaction of Ti dioxide with hydrofluoric acid. *Russian Chem Bull* **11**, 361–364.

Cao, W. & Hench, L.L. (1996). Bioactive materials. *Ceramics Int* **22**, 493–507.

Cooper, L.F. (2000). A role for surface topography in creating and maintaining bone at Ti endosseous implants. *J Prosth Dent* **84**, 522–534.

De veij, M., Vandenabeele, P., De beer, T., Remonc, J.P. & Moens, L. (2009). Reference database of Raman spectra of pharmaceutical excipients. *J Raman Spectrosc* **40**, 297–307.

Degasne, I., Baslé, M.F., Demais, V., Huré, G., Lesourd, M., Grolleau, B., Mercier, L. & Chappard, D. (1999). Effects of roughness, fibronectin and vitronectin on attachment, spreading, and proliferation of human osteoblast-like cells (Saos-2) on Ti surfaces. *Calcif Tissue Int* **64**, 499–507.

Eanes, E.D., Gillessen, I.H. & Posner, A.S. (1965). Intermediate states in the precipitation of hydroxyapatite. *Nature* **208**, 365–367.

Gandolfi, M.G., Taddei, P., Siboni, F., Modena, E., Ciapetti, G. & Prati, C. (2011*a*). Development of the foremost light-curable calcium-silicate mta cement as root-end in oral surgery. Chemical-physical properties, bioactivity and biological behaviour. *Dent Mater* **27**, e134–e157.

Gandolfi, M.G., Taddei, P., Tinti, A., Dorigo, De., Stefano, E. & Prati, C. (2011*b*). Alpha-TCP improves the apatite-formation ability of calcium-silicate hydraulic cement soaked in phosphate solutions. *Mater Sci Eng C* **31**, 1412–1422.

Gandolfi, M.G., Taddei, P., Modena, E., Siboni, F. & Prati, C. (2013). Biointeractivity-related versus chemi/physisorption-related apatite precursor-forming ability of current root end filling materials. *J Biomed Mater Res B* **101**, 1107–1123.

Gandolfi, M.G., Taddei, P., Tinti, A., Dorigo, De., Stefano, E., Rossi, P.L. & Prati, C. (2010). Kinetics of apatite formation on a calcium-silicate cement for root-end filling during ageing in physiological-like phosphate solutions. *Clin Oral Invest* **14**, 659–668.

Gehrke, S.A. & do nascimento, P.C. (2013). Analysis of bone tissue healing around ti implant surface treated with *tio* sandblasted after three and six weeks used different histological methods – a study in rabbits. *Sci J Med Clin Trials* **150**, 34–40.

Gil, F.J., Manzanares, N., Badet, A., Aparicio, C. & Ginebra, M.P. (2014). Biomimetic treatment on dental implants for short-term bone regeneration. *Clin Oral Invest* **18**, 59–66.

Guo, J., Padilla, R.J., Ambrose, W., De kok, I.J. & Cooper, L.F. (2007). The effect of hydrofluoric acid treatment of TiO2 grit blasted Ti implants on adherent osteoblast gene expression in vitro and in vivo. *Biomaterials* **28**, 5418–5425.

Hanawa, T., Kon, M., Ukai, H., Murakami, K., Miyamoto, Y. & Asaoka, K. (1997). Surface modification of Ti in calcium-ion-containing solutions. *J Biomed Mater Res A* **34**, 273–278.

Hench, L.L. & Wilson, J. (1984). Surface-active biomaterials. *Science* **226**, 630–636.

Hori, N., Iwasa, F., Ueno, T., Takeuchi, K., Tsukimura, N., Yamada, M., Hattori, M., Yamamoto, A. & Ogawa, T. (2010). Selective cell affinity of biomimetic micro-nano-hybrid structured TiO2 overcomes the biological dilemma of osteoblasts. *Dent Mater* **26**, 275–287.

Hubbs, F., Minhas, N.S., Jones, W., Greskevitch, M., Battelli, L.A., Porter, D.W., Goldsmith, W.T., Frazer, D., Landsittel, D.P., Ma, J.Y.C., Barger, M., Hill, K., Schwegler-berry, D., Robinson, V.A. & Castranova, V. (2001). Comparative pulmonary toxicity of 6 abrasive blasting agents. *Toxicol Sci* **61**, 135–143.

Iezzi, G., Vantaggiato, G., Shibli, J.A., Fiera, E., Falco, A., Piattelli, A. & Perrotti, V. (2012). Machined and sandblasted human dental implants retrieved after 5 years: A histologic and histomorphometric analysis of three cases. *Quintess Int* **43**, 287–292.

Kang, B.S., Sul, Y.T., Oh, S.J., Lee, H.J. & Albrektsson, T. (2009). XPS, AES and SEM analysis of recent dental implants. *Acta Biomaterialia* **5**, 2222–2229.

Khang, D., Lu, J., Yao, C., Haberstroh, K.M. & Webster, T.J. (2008). The role of nanometer and sub-micron surface features on vascular and bone cell adhesion on Ti. *Biomaterials* **29**, 970–983.

Kilpadi, D.V., Raikar, G.N., Liu, J., Lemons, J.E., Vohra, Y. & Gregory, J.C. (1998). Effect of surface treatment on unalloyed Ti implants: Spectroscopic analyses. *J Biomed Mater Res A* **40**, 646–659.

Kubo, K., Tsukimura, N., Iwasa, F., Ueno, T., Saruwatari, L., Aita, H., Chiou, W.A. & Ogawa, T. (2009). Cellular behavior on TiO2 nanonodular structures in a micro-to-nanoscale hierarchy model. *Biomaterials* **30**, 5319–5329.

Lamolle, S.F., Monjo, M., Lyngstadaas, S.P., Ellingsen, J.E. & Haugen, H.J. (2009*a*). Ti implant surface modification by cathodic reduction in hydrofluoric acid: Surface characterization and in vivo performance. *J Biomed Mater Res A* **88**, 581–588.

Lamolle, S.F., Monjo, M., Rubert, M., Haugen, H.J., Lyngstadaas, S.P. & Ellingsen, J.E. (2009*b*). The effect of hydrofluoric acid treatment of Ti surface on nanostructural and chemical changes and the growth of MC3T3-E1 cells. *Biomaterials* **30**, 736–742.

Le guèhennec, L., Soueidan, A., Layrolle, P. & Amouriq, Y. (2007). Surface treatments of Ti dental implants for rapid osseointegration. *Dent Mater* **23**, 844–854.

Liu, X., Chu, P.K. & Ding, C. (2004). Surface modification of Ti, Ti alloys, and related materials for biomedical applications. *Mater Sci Eng R* **47**, 49–121.

Lu, X. & Leng, Y. (2005). Theoretical analysis of Ca/P precipitation in simulated body fluid. *Biomaterials* **26**, 1097–1108.

Martinez-ramirez, S., Sanchez-cortes, S., Garcia ramos, J.V., Domingo, C., Fortes, C. & Blanco-varela, M.T. (2003). Micro-Raman spectroscopy applied to depth profiles of carbonates formed in lime mortar. *Cem Concr Res* **33**, 2063–2068.

Masaki, C., Schneider, G.B., Zaharias, R., Seabold, D. & Stanford, C. (2005). Effects of implant surface microtopography on osteoblast gene expression. *Clin Oral Impl Res* **16**, 650–656.

Massaro, C., Rotolo, P., De riccardis, F., Milella, E., Napoli, A., Wieland, M., Textor, M., Spencer, N.D. & Brunette, D.M. (2002). Comparative investigation of the surface properties of commercial Ti dental implants. Part I: Chemical composition. *J Mater Sci: Mater Med* **13**, 535–548.

Muzzarelli, R.A.A., Biagini, G., Mattioli belmonte, M., Talassi, O., Gandolfi, M.G., Solmi, R., Carraro, S., Giardino, R., Fini, M. & Nicoli aldini, N. (1997). Osteoinduction by chitosan-complexed BMP: Morpho-structural responses in an osteoporotic model. *J Bioact Compat Polym* **12**, 321–329.

Narayanan, R., Seshadri, S.K., Kwon, T.Y. & Kim, K.H. (2008). Ca/P-based coatings on Ti and its alloys. *J Biomed Mater Res B* **85**, 279–299.

Nelson, D.G.A. & Featherstone, J.D.B. (1982). Preparation, analysis and characterization of carbonated apatites. *Calcif Tissue Int* **34**, S69–S75.

Ohsaka, T., Izumi, F. & Fujiki, Y. (1978). Raman spectrum of anatase, TiO_2. *J Raman Spectrosc* **7**, 321–324.

Piattelli, A., Artese, L., Penitente, E., Iaculli, F., Degidi, M., Mangano, C., Shibli, A.J., Coelho, P.G., Perrotti, V. & Iezzi, G. (2014). Osteocyte density in the peri-implant bone of implants retrieved after different time periods (4 weeks to 27 years). *J Biomed Mater Res B* **102**, 239–243.

Racine, B., Ferrari, A.C., Morrison, N.A., Hutchings, I., Milne, W.I. & Robertson, J. (2001). Properties of amorphous carbon–silicon alloys deposited by a high plasma density source. *J Appl Phys* **90**, 5002–5012.

Raynaud, S., Champion, E., Bernache-assollant, D. & Thomas, P. (2002). Ca/P apatites with variable Ca/P atomic ratio I. Synthesis, characterisation and thermal stability of powders. *Biomaterials* **23**, 1065–1072.

Straumanis, M.E. & Chen, P.C. (1951). The mechanism and rate of dissolution of Ti in hydrofluoric acid. *J Electrochem Soc* **98**, 234–240.

Svetina, M., Colombi, L., Sbaizero, O. & Meriani, S.A.D. (2001). Deposition of calcium ions on rutile (110): A first-principles investigation. *Acta Materialia* **49**, 2169–2177.

Taddei, P., Tinti, A., Bottura, G. & Bertoluzza, A. (2000). Vibrational spectroscopic characterization of new Ca/P bioactive coatings. *Biopolymers* **57**, 140–148.

Takadama, H., Kim, H.M., Kokubo, T. & Nakamura, T. (2001*a*). An X-ray photoelectron spectroscopy study of the process of apatite formation on bioactive Ti metal. *J Biomed Mater Res A* **55**, 185–193.

Takadama, H., Kim, H.M., Kokubo, T. & Nakamura, T. (2001*b*). TEM-EDX study of mechanism of bonelike apatite formation on bioactive Ti metal in simulated body fluid. *J Biomed Mater Res A* **57**, 441–448.

Tanahashi, M. & Matsuda, T. (1997). Surface functional group dependence on apatite formation on self-assembled monolayers in a simulated body fluid. *J Biomed Mater Res A* **34**, 305–315.

Textor, M., Sittig, C., Frauchiger, V., Tosatti, S. & Brunette, D.M. (2011). Properties and biological significance of natural oxide films on Ti and its alloys. In *Ti in Medicine*, Brunette, D. M., Tengvall, P., Textor, M. & Thomsen, P. (Eds.), pp. 171–230. Berlin, Germany: Springer.

Tsukimura, N., Yamada, M., Iwasa, F., Minamikawa, H., Att, W., Ueno, T., Saruwatari, L., Aita, H., Chiou, W.A. & Ogawa, T. (2011). Synergistic effects of UV photofunctionalization and micro-nano hybrid topography on the biological properties of Ti. *Biomaterials* **32**, 4358–4368.

Tuinstra, F. & Koenig, J.L. (1970). Raman spectrum of graphite. *J Chem Phys* **53**, 1126–1130.

Vandenabeele, P., Wehling, B., Moens, L., Edwards, H., De reu, M. & Van hooydonk, G. (2000). Analysis with micro-Raman spectroscopy of natural organic binding media and varnishes used in art. *Anal Chim Acta* **407**, 261–274.

Variola, F., Yi, J.H., Richert, L., Wuest, J.D., Rosei, F. & Nanci, A. (2008). Tailoring the surface properties of Ti6Al4V by controlled chemical oxidation. *Biomaterials* **29**, 1285–1298.

Wang, L. & Nancollas, G.H. (2008). Calcium orthophosphates: Crystallization and dissolution. *Chem Reviews* **108**, 4628–4669.

Wen, H.B., de wijn, J.R., Liu, Q., De groot, K. & Cui, F.Z. (1997). A simple method to prepare Ca/P coatings on Ti6Al4V. *J Mater Sci: Mat Med* **8**, 765–770.

Wopenka, B. & Pasteris, J.D. (2005). A mineralogical perspective on the apatite in bone. *Mater Sci Eng C* **25**, 131–143.

Yamada, M., Ueno, T., Tsukimura, N., Ikeda, T., Nakagawa, K., Hori, N., Suzuki, T. & Ogawa, T. (2012). Bone integration capability of nanopolymorphic crystalline hydroxyapatite coated on Ti implants. *Int J Nanomed* **7**, 859–873.

Yang, B.C., Weng, J., Li, X.D. & Zhang, X.D. (1999). The order of calcium and phosphate ion deposition on chemically treated Ti surfaces soaked in aqueous solution. *J Biomed Mater Res A* **47**, 213–219.